Building and Environment 250 (2024) 111167

Contents lists available at ScienceDirect

Building and Environment

journal homepage: www.elsevier.com/locate/buildenv

Experimental investigation of scalar dispersion in indoor spaces

H.D. Lim [a], Timothy G. Foat [b,c], Simon T. Parker [b], Christina Vanderwel [c,*]

[a] School of Civil, Aerospace and Design Engineering, University of Bristol, BS8 1TR, United Kingdom
[b] Defence Science and Technology Laboratory, Salisbury, United Kingdom
[c] Department of Aeronautical and Astronautical Engineering, University of, Southampton, SO16 7QF, United Kingdom

ARTICLE INFO

Dataset link: https://doi.org/10.5258/SOTON/D2932

Keywords:
Indoor airflow
Eddy diffusivity
Scalar dispersion
Indoor air quality
Risk assessment

ABSTRACT

The scalar dispersion from point sources in indoor spaces is experimentally investigated using simultaneous particle–image velocimetry and planar laser-induced fluorescence techniques in a 20:1 and a 60:1 full-to-model scale room model. The ventilation inlets dominate turbulence production, with magnitudes of the velocities and Reynolds stresses observed to increase with air changes per hour (ACH). Mean concentration maps show a dependence on the ACH and source location which is attributed to the flow field at the near-source region. The peak-to-mean concentration shows a weak dependence on the mean concentration and concentration variance maps, indicating risk for toxic chemicals may be underpredicted if based only on these information. The concentration PDFs are generally well-described by exponential distributions with C_{99}/c'_{rms} values never exceeding 5.0. The magnitudes of the advective and turbulent scalar fluxes are strongly dependent on the ACH and source location, neither of which are able to dominate the other by more than an order of magnitude. The eddy diffusivity tensor was measured and a conditional-averaging based method is proposed to approximate it to an isotropic eddy diffusion coefficient, K. For real applications where K is used to estimate magnitudes of the turbulent scalar flux using the gradient transport model, the assumption of isotropic turbulence can introduce an uncertainty of around 17.8%.

1. Introduction

Air pollution is the one of the greatest environmental risks to public health and well-being. Indoor air quality (IAQ) in particular, is important as people spend a disproportionate 93% of their time indoors where the concentration of air pollutants are often higher than outdoors [1]. Nonetheless, our current understanding of turbulent mass transport and capabilities to predict scalar dispersion in indoor spaces is limited.

The Reynolds-averaged advection–diffusion equation, as shown in Eq. (1), describes the transport of the time-averaged (mean) concentration ($\overline{C}$) of a species, where $\overline{C} = C - c'$, with C representing the instantaneous concentration and c' the instantaneous concentration fluctuation. The molecular diffusion coefficient, γ, is small, and the molecular diffusion term is negligible as it is many orders of magnitude smaller than the other terms for cases of interest. For non-reacting and non-depositing species, the source term is zero everywhere except at the source location itself, and the RHS of Eq. (1) can therefore be simplified to zero:

$$\frac{\partial \overline{C}}{\partial t} + \underbrace{\overline{U_i}\frac{\partial \overline{C}}{\partial x_i}}_{\text{mean advection}} + \underbrace{\frac{\partial \overline{c'u'_i}}{\partial x_i}}_{\text{eddy diffusion}} = \underbrace{\gamma\frac{\partial^2 \overline{C}}{\partial x_i \partial x_i}}^{0}_{\text{molecular diffusion}} + \underbrace{\overline{S}}^{0}_{\text{source}}. \tag{1}$$

Eq. (1) represents the mass conservation of the species, and at steady state conditions where $\frac{\partial \overline{C}}{\partial t} = 0$, the total material entering and leaving a control volume through the mean advection and eddy diffusion transport mechanisms must therefore be equivalent. To close Eq. (1), the turbulent scalar fluxes ($\overline{c'u'_i}$) can be modelled using a gradient transport model:

$$-\overline{c'u'_i} = D_{ij}\frac{\partial \overline{C}}{\partial x_j}, \tag{2}$$

where D_{ij} represents the turbulent (eddy) diffusivity tensor [2]. A key assumption is that the turbulence length scales responsible for the scalar transport are much smaller than that of the scalar gradient. The gradient transport model is analogous to the Boussinesq's turbulent viscosity model used to close the Reynolds stresses in the

* Corresponding author.
E-mail address: c.m.vanderwel@soton.ac.uk (C. Vanderwel).

https://doi.org/10.1016/j.buildenv.2024.111167
Received 25 August 2023; Received in revised form 27 December 2023; Accepted 4 January 2024
Available online 6 January 2024

Reynolds-averaged Navier–Stokes equation:

$$-\overline{u_i'u_j'} = \nu_t\left(\frac{\partial\overline{U_i}}{\partial x_j}+\frac{\partial\overline{U_j}}{\partial x_i}\right)-\frac{2}{3}k\delta_{ij}, \tag{3}$$

where ν_t is the turbulent (eddy) viscosity, $\left(\frac{\partial\overline{U_i}}{\partial x_j}+\frac{\partial\overline{U_j}}{\partial x_i}\right)$ is the mean rate of strain tensor, k is the turbulent kinetic energy and δ_{ij} is the Kronecker delta function.

Accurate estimation of D_{ij} (or $K\delta_{ij} = D_{ij}$, for isotropic turbulence [3], where K represents the eddy diffusion coefficient) is essential for Reynolds-averaged Navier–Stokes (RANS) and analytical scalar dispersion models to accurately capture scalar dispersion rates. Nonetheless, the appropriate values remain an area of active research as it is not a fluid property but a flow property that can vary in space and time. This is particularly challenging for indoor airflows where building functionality requirements, architecture and interior design styles often lead to complex indoor airflows that do not have a clearly defined flow and scalar dispersion patterns in large volumes of the room [4–6], which results in problem-specific measurements of the eddy diffusivity.

To further complicate the problem, theoretical proof by Calder [7] has shown D_{ij} cannot be diagonal except in isotropic turbulence. Past experiments on constant mean temperature gradients in homogeneous turbulent shear flow [8] and an elevated point source plume in uniformly sheared flow [9] have also demonstrated strong evidence of an anisotropic D_{ij}. For models that rely on the gradient transport model and which assume an isotropic K to predict scalar dispersion, uncertainties are inevitably introduced, and understandably so, in order to implement engineering solutions.

There are several different methods to measure or estimate D_{ij}. Eq. (2) can be rewritten in Cartesian coordinates without loss of generality as:

$$-\overline{c'u'} = D_{xx}\frac{\partial\overline{C}}{\partial x}+D_{xy}\frac{\partial\overline{C}}{\partial y}+D_{xz}\frac{\partial\overline{C}}{\partial z}, \tag{4}$$

$$-\overline{c'v'} = D_{yx}\frac{\partial\overline{C}}{\partial x}+D_{yy}\frac{\partial\overline{C}}{\partial y}+D_{yz}\frac{\partial\overline{C}}{\partial z}, \tag{5}$$

$$-\overline{c'w'} = D_{zx}\frac{\partial\overline{C}}{\partial x}+D_{zy}\frac{\partial\overline{C}}{\partial y}+D_{zz}\frac{\partial\overline{C}}{\partial z}, \tag{6}$$

where u', v' and w' are fluctuating velocity components corresponding to directions x, y and z respectively. These equations show measurements of the mean concentration gradients and turbulent scalar fluxes are required to determine the eddy diffusivity.

Understanding the effects of turbulence on the eddy diffusivity is important in many practical applications as it is used extensively in RANS and analytical scalar dispersion models. Using simultaneous particle–image velocimetry (PIV) and planar laser-induced fluorescence (PLIF) measurements, Vanderwel & Tavoularis [9] observed counter-gradient streamwise diffusion which was attributed to the mean plume spread and its meandering motion. They showed even for steady-state flow, the dynamic flow behaviour has an influence on the measured D_{ij}, which is likely due to the larger length-scales of the plume meandering as compared to the mean concentration gradient. Counter-gradient diffusion has also been observed in large-eddy simulations (LES) of room airflow [10]. While this suggests the use of standard gradient diffusion hypothesis in RANS approaches can lead to greater uncertainties in the prediction of turbulent mass fluxes, van Hooff et al. [10] also showed RANS can provide good estimation of the predicted mean concentration levels if mean advective mass fluxes dominate over the turbulent mass fluxes.

Lim & Vanderwel [11] performed simultaneous PIV-PLIF measurements on a ground-level point source in a turbulent boundary layer flow, and showed the streamwise and wall-normal turbulent scalar fluxes are both predominantly driven by the wall-normal concentration gradient. Although the turbulent Schmidt number ($Sc_t = \nu_t/K$) is known to vary in space with no universal value across different applications [12], Lim & Vanderwel [11] showed that their measured Sc_t was still relatively close to unity and therefore, if the eddy viscosity is known it could be used to estimate the eddy diffusivity for a turbulent boundary layer flow.

Thus far, the eddy diffusivity tensor/coefficient is discussed in the context of the *advection–diffusion equation* as shown in Eq. (1), therefore it only encompasses the turbulent transport. However, in the IAQ literature, there is an alternative approach to estimate the eddy diffusion coefficient, which is based on the solutions to the *diffusion equation* (Fick's second law). In this approach, there is an assumption that there is negligible mean flow advection [13,14]. As such, estimates of the eddy diffusion coefficients obtained by matching model predictions to real-world measurements inherently combines the scalar transport mechanisms associated with both mean advection (due to mean flow patterns and large-scale turbulence) and eddy diffusion (due to small-scale turbulence). Strictly speaking, these models do not actually neglect the mean flow advection, but rather, they assume the presence of any large-scale flow structures or mean flow pattern have an isotropic and homogeneous effect on the scalar transport.

It is evident that there is a discrepancy in several past works (including our own) on whether the eddy diffusion coefficient encompasses both advective and turbulent transport [13–15] or turbulent transport only [9,11]. This highlights the importance of using different terminologies for the 'eddy diffusion coefficient', depending on whether it is based on the advection–diffusion equation or the diffusion equation. Henceforth, we will use the term 'eddy diffusion coefficient' (K) for methods based on the advection–diffusion equation approach [9,11] and the term '*total* eddy diffusion coefficient' (K_{total}) for methods based on the diffusion equation approach [15].

Mingotti et al. [16] performed an experimental study on the repeated passage of a single cylinder in a channel and presented an empirical formulation for the total eddy diffusion coefficient as a function of the frequency of oscillation, diameter of cylinder and width of the channel. Cheng et al. [14] used the eddy diffusion model, which is based on the analytical solutions to the diffusion equation with image sources to satisfy no-flux boundary conditions at the walls [13], to obtain the total eddy diffusion coefficient (K) by matching predictions from the model to real-world point measurements of the continuous release of carbon monoxide in two different rooms. They reported total eddy diffusion coefficient estimates of $K \sim 10^{-3}$ m^2 s^{-1} at air changes per hour (ACH) < 1 h^{-1} and $K \sim 10^{-2}$ m^2 s^{-1} at ACH ~ 5.4 h^{-1}. Shao et al. [17] matched the point measurements of concentrations with predictions from the eddy diffusion model and reaffirmed a clear relationship exists between ACH and K. Foat et al. [15] investigated a mechanically ventilated room and estimated $K \sim O(10^{-2}$ m^2 s$^{-1})$ using the turbulent kinetic energy balance [18], and suggested it is dependent only on the room volume, room flow rate and number of supply vents.

Although the eddy diffusion model has been shown to be valid in many indoor airflow scenarios [14,15,17], its accuracy is strongly dependent on selecting the right value of the total eddy diffusion coefficient. A survey of the literature revealed there is a large variation in the appropriate values to use for the total eddy diffusion coefficient for indoor air flows, with a lower limit of 1×10^{-3} m^{2}s^{-1} [19] to an upper limit of 1.9×10^{-1} m^{2}s^{-1} [13]. This can have a very significant impact on the accuracy of scalar dispersion models. As such, characterising its value and associated uncertainty for different indoor air flow configurations is very important for practical applications.

Despite recent advances in the fundamental understanding of indoor airflow [20,21], there is very limited literature focusing on the scalar transport mechanism and eddy diffusivity in a realistic room model with complex flow (i.e. weak forced advection and Re-dependent flow in the occupied region of the room [22–24]). This is because of the difficulty to validate numerical simulations due to limited availability of high-fidelity experimental datasets. In this study, we make use of recent advances in PIV and PLIF techniques to study the effects of source location and ACH on the scalar transport mechanism and eddy

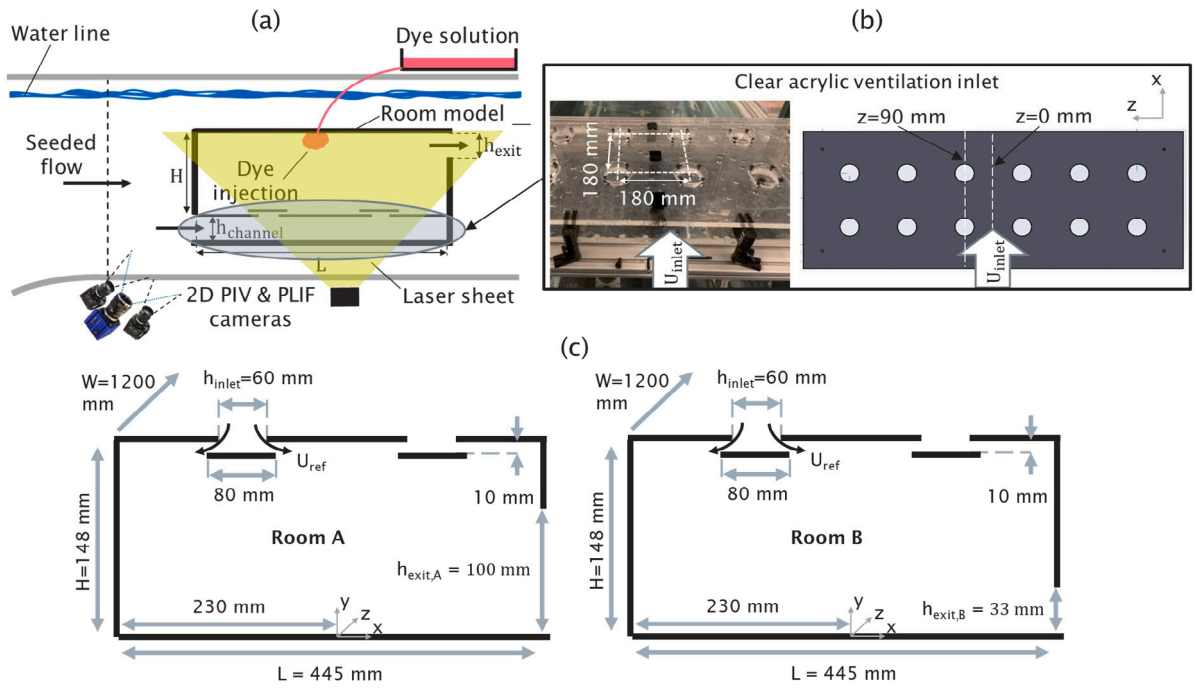

Fig. 1. Schematic of the (a) experimental setup with the room model mounted in an upside down configuration, (b) the ventilation inlet and (c) room models A and B.

diffusivity in scaled room models in a water flume facility. To the best of the authors' knowledge, this is the first time spatially-resolved experimental measurements of the advective and turbulent scalar fluxes and the eddy diffusivity are presented for this particular flow application.

The layout of our manuscript is as follows. In Section 2, we present details on the methodology, room model and test parameters. In Section 3, spatially-resolved velocity and concentration statistics are presented. Section 4 focuses on the turbulent scalar fluxes and the influence of the mean advective flow on mass transport. In Section 5, measurements of the eddy diffusivity tensor are presented, and a methodology to approximate it to an isotropic eddy diffusion coefficient with an associated uncertainty is proposed. Section 6 presents the conclusions of our study.

2. Experimental methodology

2.1. Setup and data acquisition

Simultaneous PLIF and PIV measurements of two scaled room models were performed in the University of Southampton's Boldrewood Campus Recirculating Water Tunnel facility. PIV and PLIF are established optical measurement techniques in the field of fluid mechanics, and rely on seeding particles and fluorescent dye as tracers respectively, to measure spatially-resolved velocity and concentration fields. The initial design of the room models was motivated by the Nielsen benchmark test case [25], which is a 2D room with a Re = 5000 wall jet slot inlet that leads to large-scale primary recirculating flow in the room. To be more consistent with realistic cases of interest, which have weaker forced advection and Re-dependent flow in the occupied region of the room [22,23], a few modifications to the room geometry and ventilation inlets and outlets were required. Nonetheless, designing these modifications was not trivial, as a survey of the literature revealed a very wide variety of room geometries and ventilation designs for indoor spaces. Even if the scope is limited to just offices or homes, ventilation designs can still differ very drastically due to differences in climate, humidity, installation costs, natural vs mechanical/hybrid ventilation systems, etc [26,27].

To strike a compromise between producing realistic room flows and maintaining a simple room geometry for subsequent studies, it was decided that the flow in the room model should be quasi-2D with periodic boundary conditions and have deflector plates at the inlet to weaken the forced advection and form ceiling jets similar to air exiting ceiling diffusers [15]. Two room models were designed, which spanned the entire width of the flume (W = 1.2 m) and have a height of H = 148 mm and length of L = 445 mm. This was fully submerged and rigidly fixed to the flume in an upside down configuration as shown in Fig. 1(a). Flow in the room model was driven by the flume which forces fresh fluid into a channel with height $h_{channel}$ = 40 mm, and through twelve h_{inlet} = 60 mm diameter circular ventilation inlets with 80 mm diameter deflector plates arranged in a 6 × 2 configuration, spaced at 180 mm apart from each other as shown in Fig. 1(c). The mixed fluid exits the room through a rectangular slot opening that spans the width of the flume and has an exit slot height of h_{exit}. This was adjusted to h_{exit} = 100 mm for room A and h_{exit} = 33 mm for room B, which represents 20:1 and 60:1 full-to-model length scale ratio ($L_{ratio,i=A,B}$) rooms respectively. Therefore, the two room models represent full-scale rooms with ceiling heights of 3 m and 9 m, with 2 m outlets similar to a quasi-2D door. The location of the origin within the room and other key geometrical dimensions are also shown in Fig. 1(c).

Rhodamine 6G dye which has a Schmidt number of Sc = 2500 ± 300 [9] was used as a passive scalar tracer and continuously released via a 2.5 mm inner diameter tube at ground level and x-locations as shown in Table 1. The fluorescent dye was fed from a Mariotte's bottle reservoir via gravity and a needle valve was used to ensure a constant dye flow rate of Q_{dye} = 10 mL min^{-1}. The source concentration was C_s = 10 mg L^{-1} for all test cases. The flume was seeded with 50 μm polyamide seeding particles and recirculated in the flume until uniform seeding and the desired seeding density was achieved in the room model. A Nd:YAG double-pulsed laser with an emission wavelength of 532 nm was used to illuminate the seeding particles and excite the fluorescent dye which has absorption and emission peaks at 525 nm and 554 nm respectively.

To separate the signals from the fluorescent dye and PIV particles, a 540 nm long-pass filter was fitted to a 5.4 MP 16-bit depth Imager sCMOS camera for the PLIF measurements and 532 nm laser-line band-pass filters were fitted to either two 4 MP Imager MX CMOS cameras or two 4 MP Phantom v641 cameras for the 2D PIV measurements,

depending on the exact test case. The PLIF single-frame and PIV double-frame acquisition frequency was either 2 Hz or 2.5 Hz depending on the exact test case, and the interframe time of the double-frame PIV images was adjusted to satisfy the one-quarter rule for optimal particle displacement for all test cases [28]. The acquisition frequency and PIV cameras were varied across different test cases as the dataset presented in this study came from multiple experimental campaigns. This had negligible effects on the results and discussions in this study. In this study, all PIV-PLIF measurement and dye release planes were at z = 0 mm, which was equidistant from two columns of ventilation inlet as shown in Fig. 1(b).

The PIV and PLIF post-processing procedures were similar to several of our recent studies [29], hence only a succinct description will be provided here. The particle images were post-processed using LaVision DaVis 10 commercial software and PIVlab 2.61 open-source software [30]. Images were pre-processed to remove background noise, before performing multi-grid multi-pass cross-correlation analysis with 50% overlap ratio to obtain a final vector resolution of 1.56 mm–1.75 mm. Spurious vectors were removed and replaced using local neighbourhood standard deviation and median filters. The velocity bias due to calibration error is estimated to be up to 0.5% and the standard error is estimated to be up to 3% at 95% confidence interval based on the standard bootstrap with replacement procedure to estimate the sampling distribution of a statistic.

For the PLIF post-processing procedure, two calibration tanks filled with dye concentrations of 0.03 mg L^{-1} and 0.05 mg L^{-1} and the background concentration were used to calibrate the fluorescence intensity to the dye concentration using an inhouse code. The two dye concentrations in the calibration tanks are in the linear response regime of the fluorescent dye. The light attenuation and temporal variations in the laser pulses were accounted for using the Beer–Lambert's law and an energy monitor respectively. The PLIF resolution is 0.174 mm–0.191 mm. A conservative estimate of the bias error is up to 10.2% at 95% confidence interval and the standard error is estimated to be up to 1% based on a bootstrap with replacement procedure. The PLIF resolution is higher than PIV resolution since the latter is limited by the finite size of the cross-correlation window. To calculate the joint velocity-concentration statistics which will be essential to examine the scalar transport mechanisms, we performed upsampling of the velocity fields to the concentration fields via linear interpolation. The propagated measurement uncertainty for joint probability statistics is up to 14.7%.

2.2. Test parameters

The scaled water flume experiments need to achieve dynamic similarity as the full-scale problem with air as the working fluid. This was achieved by matching the Reynolds number based on U_{ref} and h_{inlet}, where U_{ref} is the average inlet velocity calculated based on the flow rate averaged over z = 0 mm and z = 90 mm. The Reynolds number based on the inlet flow was selected because the production of mechanical turbulence in the room is expected to be dominated by the ventilation inlet [31]. Nonetheless, it is acknowledged that the flow in an indoor space is very complex and a single room can have drastically different flow dynamics in different parts of the room, including jet flows, boundary layer flows, separated flows, recirculation zones, laminar, low turbulent or fully developed turbulent flows [20,22,32]. As such, there is really no single non-dimensional parameter that can fully describe complex flows in realistic rooms.

The ventilation time scale is calculated by taking the volume of the room divided by the room flow rate, and the full-to-model ventilation time scale ratios ($t_{ratio,i=A,B}$) can therefore be calculated as 26.7 and 240 for rooms A ($L_{ratio,A}$ = 20) and B ($L_{ratio,B}$ = 60) respectively. Accordingly, these time and length scale ratios can be used to convert quantities in model scale to full scale for the rest of the study.

Table 1
Test parameters for rooms A and B with subscript FS denoting quantities at full-scale.

Test case	U_{exit} [m s^{-1}]	U_{ref} [m s^{-1}]	$U_{ref,FS}$ [m s^{-1}]	Re_{inlet}	ACH_{FS} [h^{-1}]	Source x-location [x/h_{exit}]
A1	0.05	0.19	0.14	11,200	10.8	0
A2	0.13	0.47	0.36	28,400	27.4	0
B1	0.23	0.28	0.07	16,500	1.8	0
B2	0.25	0.29	0.07	17,400	1.9	0
B2-L	0.25	0.29	0.07	17,400	1.9	−3.5
B2-R	0.25	0.29	0.07	17,400	1.9	3.5
B3	0.28	0.33	0.08	19,800	2.1	0
B4	0.34	0.40	0.10	24,100	2.6	0
B5	0.37	0.44	0.11	26,100	2.8	0

For instance, to convert the model reference velocity U_{ref} to full-scale reference velocity $U_{ref,FS}$, the full-to-model length ratio and the full-to-model time ratio can be applied as such:

$$U_{ref,FS} = U_{ref} \times \frac{L_{ratio}}{t_{ratio}}. \quad (7)$$

Table 1 shows the experimental parameters investigated in this study with the subscript FS added to quantities that have been converted to full-scale. The full-scale reference velocities are consistent with the observations by King et al. [33], where flow velocities from an inlet diffuser were observed to be up to 0.7 m s^{-1}. The ACH_{FS} values are representative of typical indoor spaces [34,35], and the Reynolds numbers are similar to some [36,37] and higher than other studies [22,25,31].

3. Velocity and concentration statistics

3.1. Mean flow fields

The mean velocity magnitudes for selected test cases are presented in Fig. 2 to illustrate the effects of increasing ACH for rooms A and B. For room A, increasing the ACH led to an increase in normalised velocity magnitudes and dissimilar flow patterns in the room particularly at around [$x/h_{exit,A}$, $y/h_{exit,A}$] = [−0.4, 0.2] (see Figs. 2a, 2b). For room B, the increase in ACH also led to an increase in normalised velocity magnitudes and changes to the room flow pattern (see Figs. 2c, 2d). Notably, the flow rate close to the right inlet has increased, resulting in flow from both inlets impinging onto each other and redirected as strong downward flow in the middle of the room. The velocity variances and Reynolds shear stress are presented in Fig. 3. Peak magnitudes are observed close to the inlet which indicate turbulence is predominantly produced there. With an increase in ACH, higher normalised magnitudes of the velocity variances and Reynolds shear stress are observed. The dependence of the velocity statistics and streamlines on the ACH indicate the flow is Re-dependent.

For the range of ACH (i.e. Re_{inlet}) investigated in this study, the room flow is not fully developed as illustrated by the streamlines in Fig. 2. This is typically the case for most modern and realistic room flows [22,23]. While some studies with idealised room geometries and less complex room flows do claim Re independence [25,37], there are several discussions on the occupied zone (in the centre of the room) being in a transitional state between turbulent and laminar, despite the jet inlet having already achieved Reynolds number that is far higher than the critical Reynolds number [24,38]. Al-Sanea et al. [37] achieved Re independence in the entire room and discussed the criteria to remain Reynolds independent is for the flow to be dominated by forced advection. In most realistic and non-specialist rooms however, it is very rare for the entire room to be dominated by forced advection.

The mean concentration fields with isocontour lines of six test cases, selected to illustrate the effects of ACH and source locations, are presented in Fig. 4. Fig. 4(a) shows the dye spreads in the radial direction away from the source rather uniformly in the near-source

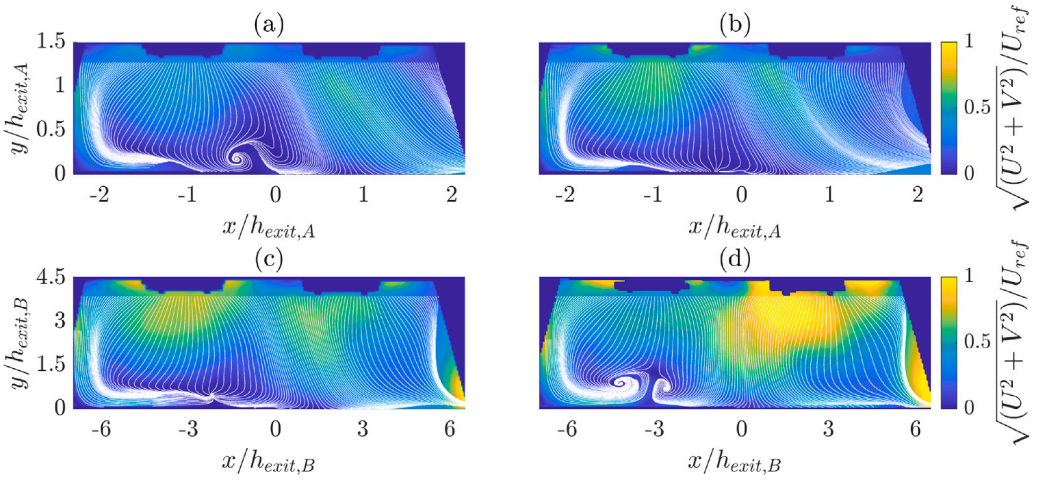

Fig. 2. Time-averaged streamlines and velocity magnitude contours for test cases (a) A1, (b) A2, (c) B2 and (d) B5.

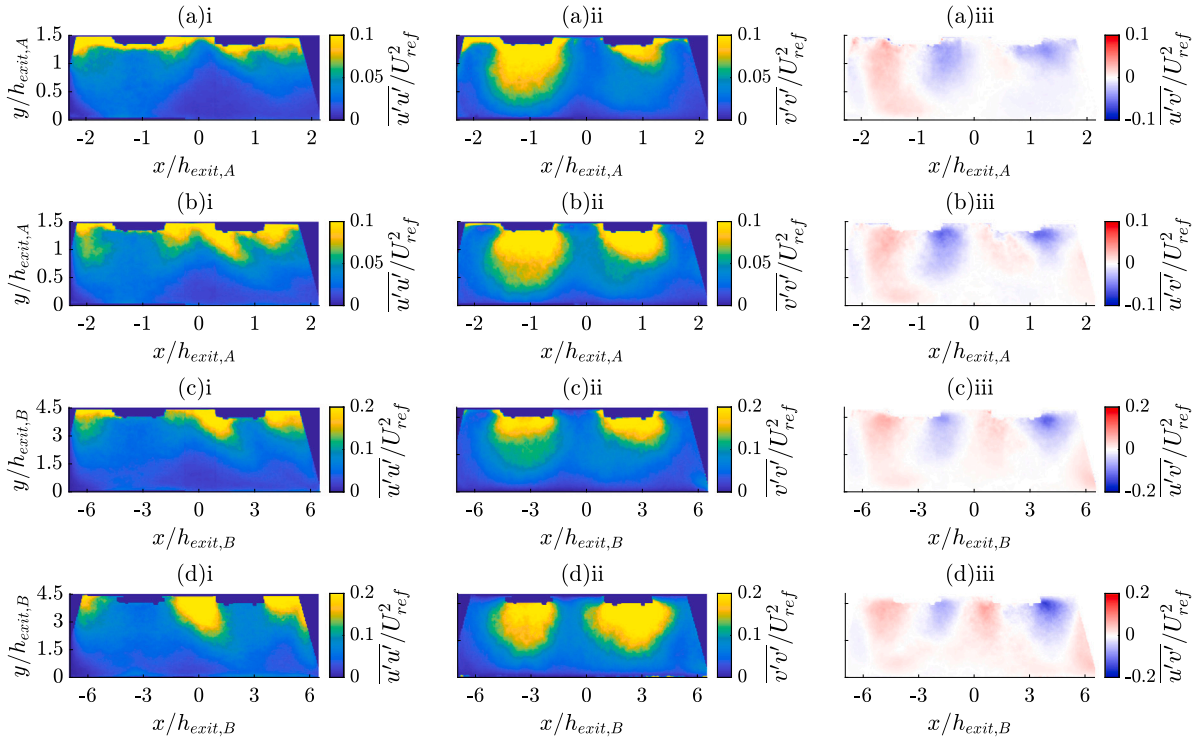

Fig. 3. Time-averaged (i) horizontal velocity variance (ii) vertical velocity variance and (iii) Reynolds shear stress for test cases (a) A1, (b) A2, (c) B2 and (d) B5.

region. The comparison with Fig. 4(b) illustrates the effect of ACH_{FS} increasing from 10.8 h^{-1} to 27.4 h^{-1} for room A, with isocontour lines changing significantly, from a semicircle to a flattened semicircle shape. Similar trends are observed for room B as the ACH_{FS} increases from 1.9 h^{-1} to 2.8 h^{-1} as shown in Fig. 4(c–d) which can be attributed to stronger downward mean flow advection near the centre of the room as shown in Fig. 2. The overall spatial distribution of the mean concentrations for both rooms A and B become more evenly mixed with an increase in ACH_{FS}.

The source location plays an important role in the mean concentration maps, as illustrated in the B2, B2-L and B2-R test cases shown in Figs. 4(c,e,f), which have the exact same boundary conditions but different source locations. For the B2-R test case where the dye enters the room at [$x/h_{exit,B}$, $y/h_{exit,B}$] = [3.5, 0], the isocontour lines (see Fig. 4(f)) are completely different to the other test cases. This is due to the strong advective flow at the outlet, which transported most of the dye out of the room directly, hence leading to negligible mean concentrations measured in the other parts of the room. This hypothesis is supported by Fig. 2(c), where the B2-R test case showed streamlines that led straight to the room outlet without an opportunity for the scalar dye to recirculate back into the room.

In contrast, when the scalar dye enters the room at [$x/h_{exit,B}$, $y/h_{exit,B}$] = [0, 0] and [−3.5, 0] for test case B2 and B2-L respectively, the streamlines in Fig. 2(c) show they are transported to a sink at approximately [$x/h_{exit,B}$, $y/h_{exit,B}$] = [−2.2, 0.5]. This explains the relatively similar 'hemisphere' shaped mean concentration contour lines observed in test cases B2 and B2-L (see Figs. 4(c) and 4(e)), which is in stark contrast to test case B2-R. The streamlines show source locations can lead to significant changes in the mean advective scalar transport mechanism at the near-source region, resulting in a much

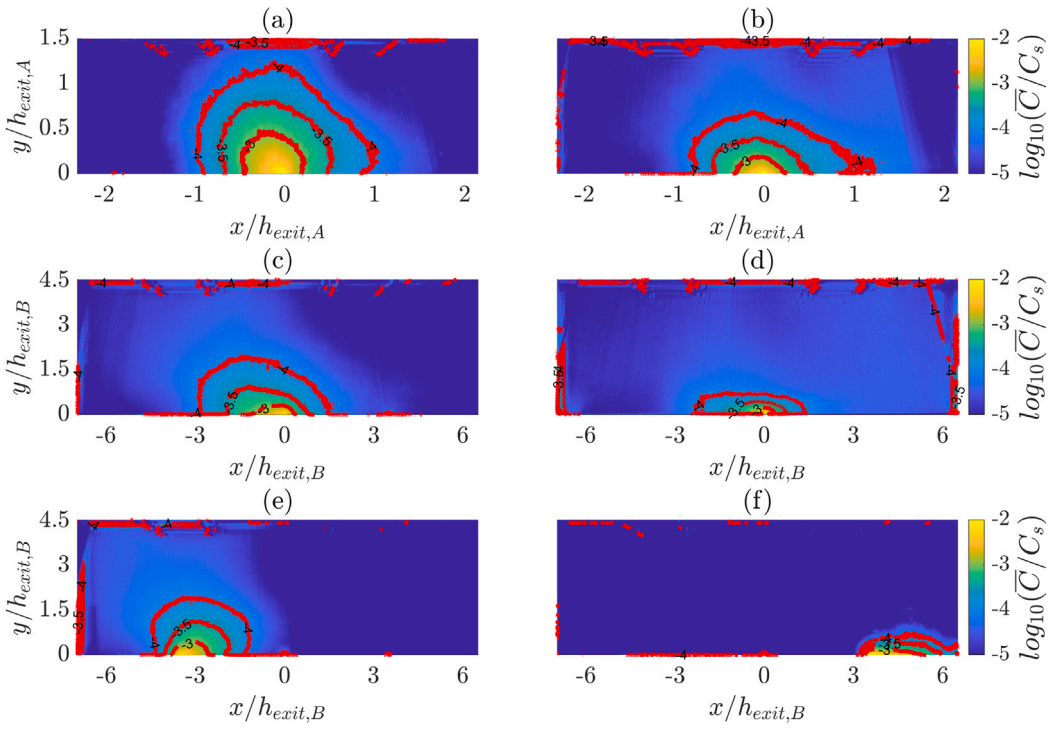

Fig. 4. Mean concentration and isocontour levels for (a) A1, (b) A2, (c) B2 and (d) B5, (e) B2-L and (f) B2-R test case.

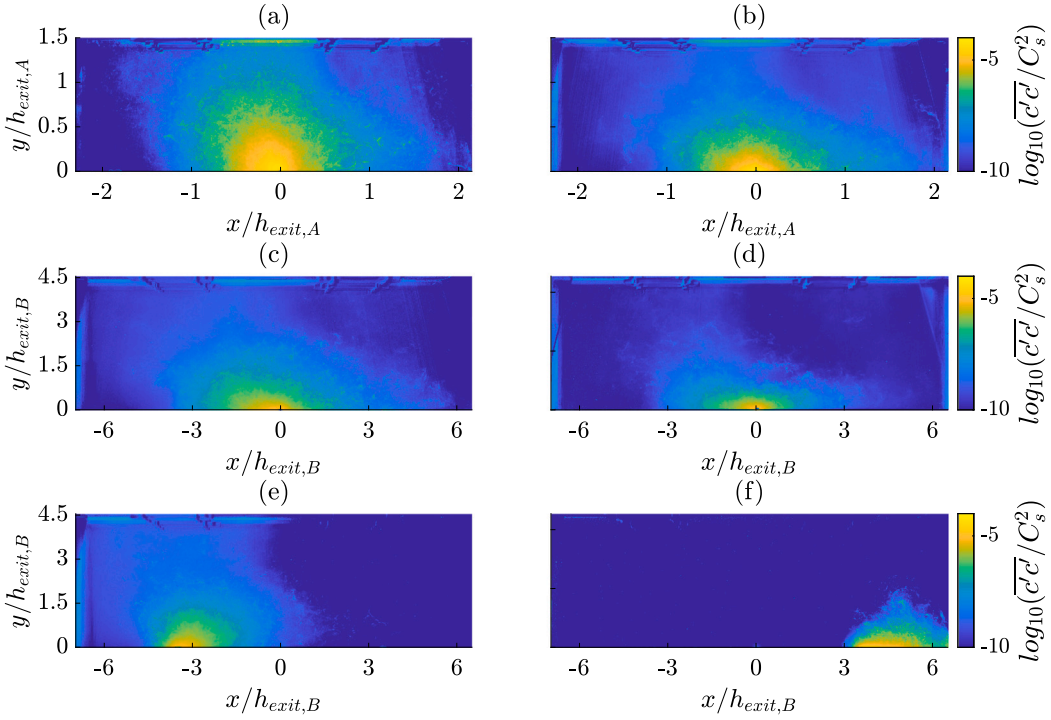

Fig. 5. Mean concentration variance for (a) A1, (b) A2, (c) B2, (d) B5, (e) B2-L and (f) B2-R test case.

more significant effect on the mean concentration maps as compared to the effects of ACH_{FS}. These observations are consistent with an earlier study that showed the relative positions of the source can have significant influences on particle distribution and deposition [39]. We will return to quantify these effect later based on our scalar flux measurements.

3.2. Concentration variances and PDFs

The concentration variance maps are presented in Fig. 5, where the largest magnitudes are measured at the source and decay with distance from source. While this effect is generally robust to changes in ACH_{FS} or source location and has also been observed for studies based on the Nielsen room [40], it is dependent on the flow field close to the source.

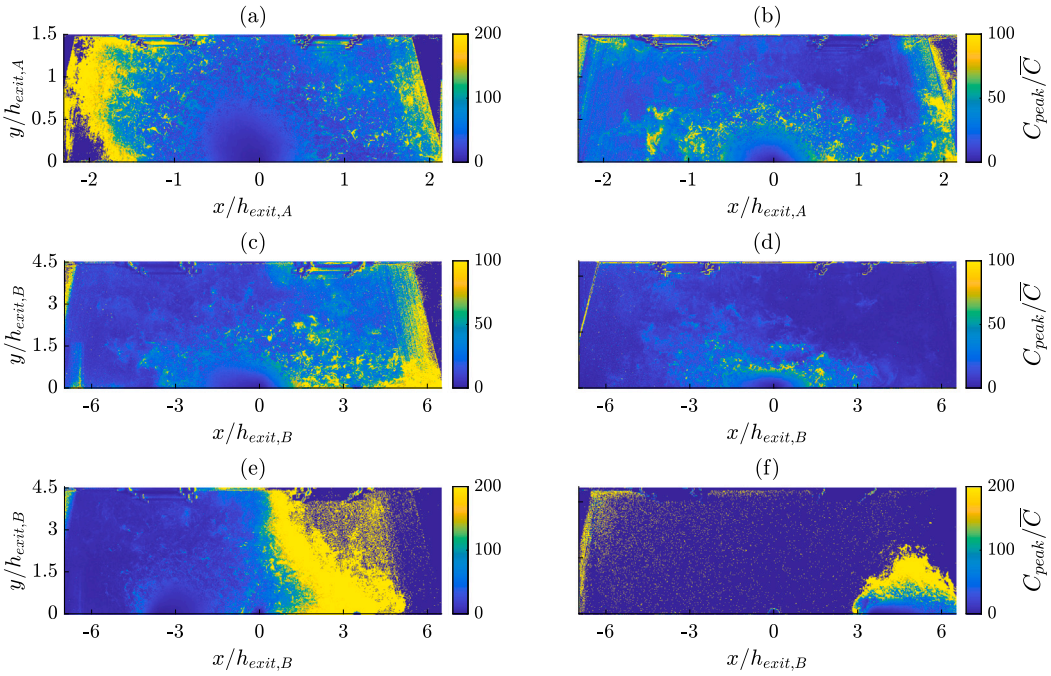

Fig. 6. Peak-to-mean concentration maps for (a) A1, (b) A2, (c) B2, (d) B5, (e) B2-L and (f) B2-R test case.

This is best exemplified by Fig. 5(f) where the proximity of the source to the outlet led to almost zero variances everywhere in the room apart from the region close to the source. In addition, the concentration variance patterns observed here are generally very similar to those of the mean concentration. An increase in the ACH_{FS} led to the flattening of the variance contours towards the ground, while the change in source location plays an important role in the concentration variance patterns in the rooms. We will discuss the connections between the concentration and velocity fluctuations later.

The peak-to-mean concentration ratio ($C_{peak}/\overline{C}$), where C_{peak} is defined as the maximum concentration measured in the entire acquisition (around 100 ventilation time for room A and 460 for room B), is an important parameter in air pollution applications where determining exposure level or risk assessments are required. It is also useful in other applications including the response of buildings to short-term outdoor hazardous pollutants [41], the assessments of practical shelter-in-place scenarios [42], explosives detection by dogs [40], assessing the response of air quality models to sharp concentration peaks [43], correlations to human activities [44] and to devise ventilation strategies [45].

In the context of security applications, for e.g. when there is an accidental or deliberate release of toxic chemicals such as chlorine or hydrogen sulphide which have high toxic load exponents (TLEs) [46], the toxic load is described by Eq. (8) [47,48] as:

$$Toxic\ load = \int_0^\infty C^m\, dt, \tag{8}$$

where m is the toxic load exponent. This equation indicates the need to consider short-duration events when determining exposures and assessing risks of toxic gases which the $C_{peak}/\overline{C}$ parameter is well-suited for. In the context of environmental sources where TLE values are close to one, Eq. (8) reduces to the Haber's rule [49], then the time-integrated concentration or conditional probabilities is useful to determine exposures.

Fig. 6 presents the $C_{peak}/\overline{C}$ maps, where it can be observed that the smallest values were actually observed close to the source where mean concentration magnitudes are the highest. For room A, the A1 test case (Fig. 6(a)) is observed to have the highest magnitudes in the left side of the room where very low mean concentration was observed. This indicates significant transport of scalars due to turbulence, which brings high concentrations of dye to the left side of the room in an intermittent manner, resulting in low mean concentration values but high $C_{peak}/\overline{C}$. As the ACH_{FS} increases from 10.8 h^{-1} to 27.4 h^{-1}, the scalar transport due to flow advection becomes more efficient, resulting in higher mean concentration values in the left side of the room and thus, lower overall $C_{peak}/\overline{C}$ values in the room (Fig. 6(b)). For room B (Fig. 6(c)), high $C_{peak}/\overline{C}$ values are observed close to the outlet and near the ground where mean concentration values are low. Similar to room A, an increase in ACH_{FS} from 1.9 h^{-1} to 2.8 h^{-1} for room B lowered the high $C_{peak}/\overline{C}$ values near the outlet, due to improved scalar mixing leading to more uniform and higher values of mean concentration fields near the outlet as shown in Fig. 4. For test case B2-L where the source is located on the left side of the room (Fig. 6(e)), high $C_{peak}/\overline{C}$ values are observed close to $x/h_{exit,B} = 3$ where very low mean concentration values were observed (Fig. 4(e)).

For the test case where the source location is located close to the outlet (Fig. 6(f)), $C_{peak}/\overline{C}$ values are essentially zero everywhere in the room, including regions with low mean concentrations as shown in Fig. 4(f), except for the near-source and outlet region where the dye was directly extracted out of the room via the outlet. The highest $C_{peak}/\overline{C}$ values are observed away from the ground where the mean concentration is lower than near to the ground (Fig. 4(f)).

The comparison between the concentration variance and $C_{peak}/\overline{C}$ maps (Figs. 5 and 6) shows a clear lack of correlation, indicating the concentration variance plays a limited role in determining the $C_{peak}/\overline{C}$ ratio. In addition, low mean concentration values are a necessary, but not the only, condition for high $C_{peak}/\overline{C}$ values. These two observations show the risk for toxic chemicals with high TLEs will be significantly underpredicted if risk assessments are based only on the mean concentration and concentration variance.

To gain deeper insights relevant to exposure and risk assessments, the concentration PDF is calculated using 1000 datapoints of concentration measurements in time (i.e. 100 and 460 ventilation times for rooms A and B respectively) extracted from 55 regular grid locations. For room A, the datapoints are extracted between the x-range $-1.25 < x/h_{exit,A} < 1.25$ at 11 regular intervals of $x/h_{exit,A} = 0.25$, and between the y-range $0.125 < y/h_{exit,A} < 0.625$ at 5 regular intervals of $y/h_{exit,A} = 0.125$. The

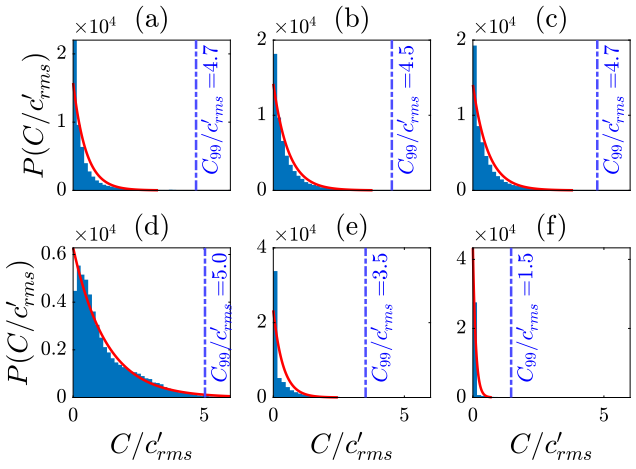

Fig. 7. Concentration PDF for (a) A1, (b) A2, (c) B2, (d) B5, (e) B2-L and (f) B2-R test case. The red line shows an exponential fit. (For interpretation of the references to colour in this figure legend, the reader is referred to the web version of this article.)

datapoints are extracted at the same locations for room B which in non-dimensional units are: $-3.788 < x/h_{exit,B} < 3.788$ at $x/h_{exit,B} = 0.758$ regular intervals and $0.379 < y/h_{exit,B} < 1.894$ at $y/h_{exit,B} = 0.379$ regular intervals.

The associated PDFs are presented in Fig. 7. These PDFs have very long right tails with the exponential distribution a good fit for most of the test cases except for B2-L and B2-R. In comparison with the gamma distribution observed in scalar plumes in turbulent boundary layers [11], the exponential distribution here indicates a larger number of low concentration events and lower number of high concentration events. Since small-scale flow structures are effective at promoting fine-scale mixing while large-scale flow structures are effective at bulk transport, an exponential distribution would suggest more intermittent large-scale flow structures that are responsible for advecting high concentrations of dye across the room.

The C_{99}/c'_{rms} parameter, defined as the ratio of the concentration value exceeded 1% of the time to the concentration fluctuations root-mean-square, is a way to measure the right tail of the distribution and useful for risk assessment. This parameter is appended to the concentration PDFs shown in Fig. 7 and generally varies between 4.5 to 5.0, but much lower values are observed for test cases B2-L and B2-R. A property of the exponential distribution is that the expected value at the 99% percentile can be derived as $C_{99}/c'_{rms} = 4.61$ (since $C_{99} = -ln(0.01)/\lambda$ and $c'_{rms} = 1/\lambda$, where λ is the rate parameter). This agrees well with the results shown in Fig. 7(a-d) which are well described by the exponential distribution. The departure from the exponential distribution for test cases B2-L and B2-R can be attributed to very low mean concentrations (see Fig. 4) measured at the sampled locations, due to the mean advective flow patterns in the near-source region. Since higher mean concentration values are expected close to the source, the distance from source (and mean flow direction if mean flow advection dominates scalar transport at the near-source region) is the most important parameter in determining the C_{99}/c'_{rms} values.

4. Concentration fluxes

4.1. Turbulent scalar fluxes

The turbulent scalar fluxes require simultaneous measurements of the instantaneous concentration and velocity fields, of which very limited experimental or field measurements are available in the literature. The mean horizontal and vertical turbulent scalar fluxes are presented in Fig. 8(i) and 8(ii) respectively. For all test cases, there is a general trend of the turbulent fluxes pointing away from the source, with their peak magnitudes decaying with distance from source. The increase in ACH_{FS} (see Figs. 8(a–b) and 8(c–d)) led to slight flattening of the fluxes towards the ground, but otherwise, has limited effect on the overall pattern of the fluxes. The change in source location (see Fig. 8(c, e, f)) has a much bigger impact on the turbulent fluxes because it introduce radical changes to the flow field close to the source. Fig. 8(f)ii in particular shows the vertical turbulent scalar flux which is similar to that of a point source ground-level plume in a turbulent boundary layer, although interestingly, the horizontal turbulent fluxes are mostly positive here which is different to the counter-gradient streamwise turbulent fluxes observed in the turbulent boundary layer [11]. Finally, we note that it is challenging to meaningfully collapse the turbulent fluxes across the different boundary conditions presented here, as the magnitudes and patterns are strongly dependent on the turbulent and mean flow field near the source.

4.2. Advective scalar fluxes

The decay of the turbulent scalar fluxes and concentration variance with distance from source indicate the near-source flow turbulence is more likely to have a larger influence on the mean concentration maps as compared to that of the far field. To have a more complete understanding of the scalar transport mechanism, it is important to also consider the advective scalar fluxes. This is particularly important for the near-source region where the mean concentration is the highest, and less so for the far field where the mean concentration has decayed significantly. Fig. 9 presents the corresponding advective fluxes for the test cases. Interestingly, as the ACH_{FS} increases for room A, the vertical advective flux in the near-source region changes direction from upward to downward (Fig. 9(a–b)), with the downward component flattened to a very thin region close to the source.

To understand this change, consider a point source in zero advective flow environment, where the radial advective fluxes are expected to be positive around the source which decays with distance from source. By introducing a wall here which enforces zero flux boundary condition, and by introducing downward advective flow close to the source (due to the room ventilation design), a gradual increase in ACH_{FS} would eventually lead to a change in vertical flux directions in the near-source region as well as a general flattening of the fluxes towards the ground. Therefore, for this particular room design and test conditions, the flow at the near-source region is strongly dependent on the ACH_{FS}. Fig. 9(c, e, f) shows very different advective flux patterns associated with the change in source location, which can be attributed to the difference in the mean flow at the near-source region (see Fig. 2). For Fig. 9(f) in particular, because of its proximity to the outlet, most of the dye advects out of the room immediately. These results indicate the flow field in the near-source region is an important factor to consider when examining the effects of ACH_{FS} or source location.

Knowing the relative magnitudes of the turbulent and advective fluxes can be useful for selecting the most suitable mathematical model to predict scalar dispersion. The relative magnitudes are shown in Fig. 10, where values greater than one represents turbulent fluxes that are at least an order of magnitude larger than its corresponding advective component, and values less than −1 represents at least an order of magnitude smaller. For the range of test cases considered in this study, the relative magnitudes at the near-source region are observed to be heavily dependent on the near-source flow conditions, which is in turn, dependent on the ACH_{FS}, source location and room geometry. As an example, the Gaussian plume model may be the most appropriate scalar dispersion model for test case B2-R, where the horizontal advective flux dominates its turbulent component while neither the advective nor turbulent vertical flux are able to dominate each other (see Fig. 10(f)). However, a simple change in source locations as shown in test cases B2 and B2-L (see Fig. 10(c,e)) clearly show this is no longer an appropriate dispersion model. As such, without any knowledge of the flow field (particularly at the near-source region), there is no universal selection

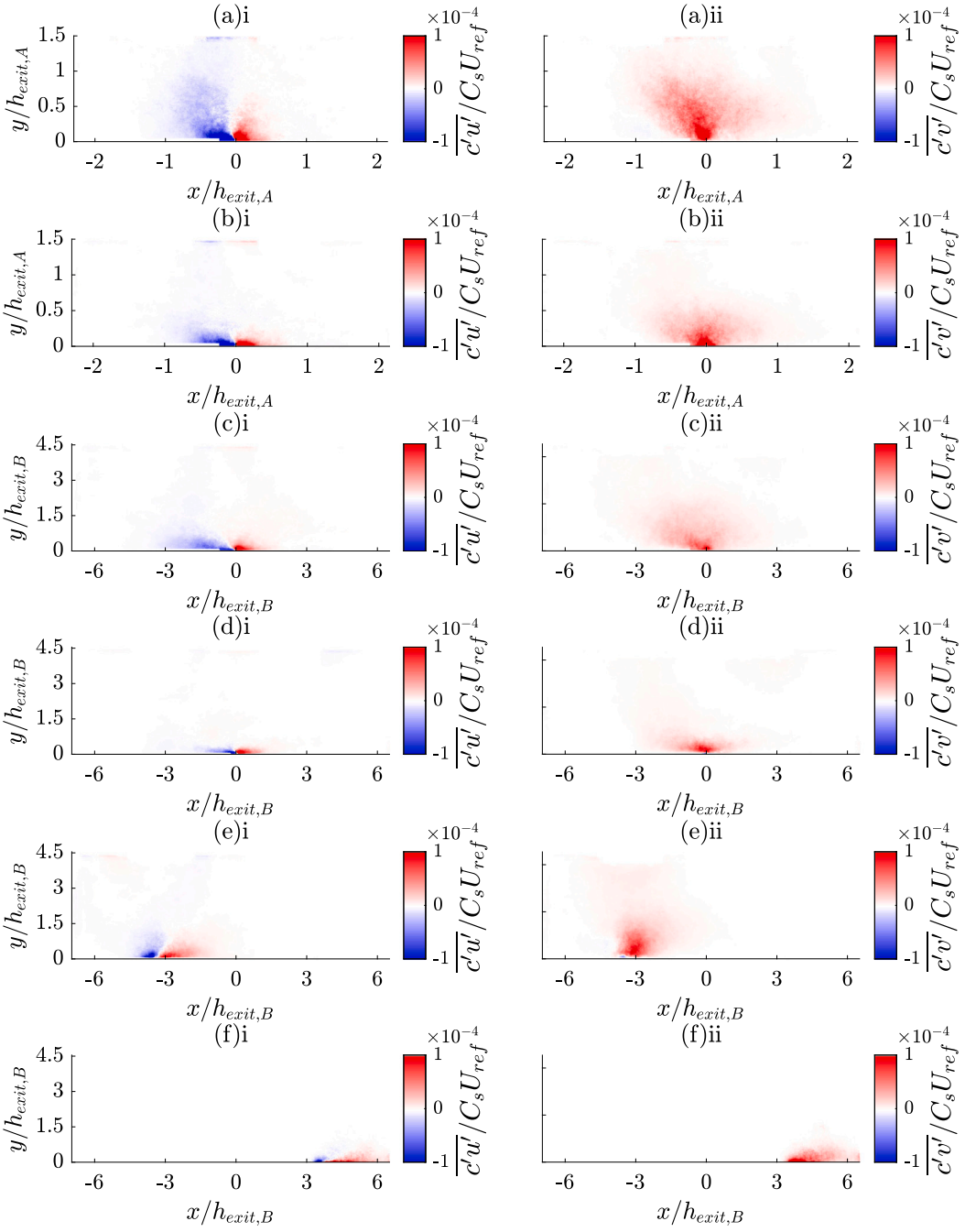

Fig. 8. Mean (i) horizontal and (ii) vertical turbulent scalar fluxes for (a) A1, (b) A2, (c) B2, (d) B5, (e) B2-L and (f) B2-R test case.

criteria for the most appropriate scalar dispersion mathematical model for indoor applications.

For a RANS approach, it is the gradients of the turbulent and advective scalar fluxes as shown in Eq. (1) that affects the mean concentration. Fig. 11 presents the ratio of this gradient, and show there is relatively larger contribution of the turbulent component at the near-source region, while far from the source, the advective component dominates. As such, for RANS to accurately estimate the mean concentration, it is important to accurately capture the turbulent scalar fluxes. This requires accurate characterisation of the eddy diffusivity which will be discussed in the next section.

5. Eddy diffusivity

For many practical applications, the eddy diffusivity is required to model scalar dispersion. As discussed in the literature review, different measurement techniques or models use different assumptions to measure the eddy diffusivity. This introduces inherent uncertainties which are often unaddressed. In this section, we present our measurements of the eddy diffusivity, a methodology to approximate measurements of the eddy diffusivity tensor with an isotropic coefficient, and discuss the associated uncertainties related to the assumption of isotropic turbulence. Furthermore, the eddy diffusion coefficients associated with changes in the boundary conditions investigated in this study will be

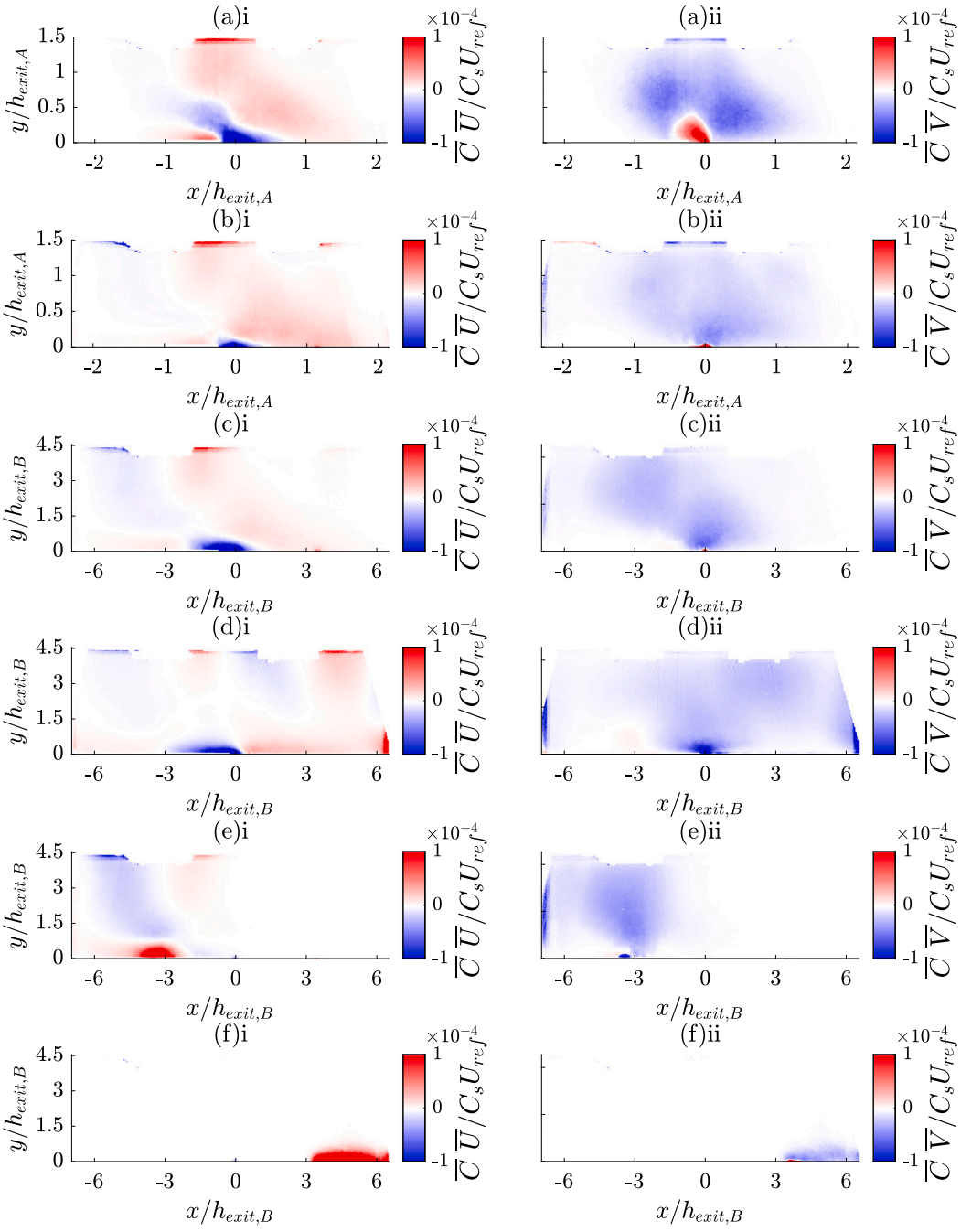

Fig. 9. Mean (i) horizontal and (ii) vertical advective scalar fluxes for (a) A1, (b) A2, (c) B2, (d) B5, (e) B2-L and (f) B2-R test case.

discussed which may be a helpful reference for future studies and engineering applications.

5.1. Components of the eddy diffusivity tensor

Consider Eqs. (4)–(6), where the turbulent scalar fluxes are presented in Cartesian coordinates as the products of the components of the eddy diffusivity tensor and the mean concentration gradients. In a room flow which can have very complex flow regimes, the direction of the turbulent scalar fluxes is strongly dependent on the spatial location. In order to understand the contributions of the principal and orthogonal components of the mean concentration gradients to the principal direction of the turbulent scalar flux, it is preferable to redefine Eq. (2) as

$$-\overline{c'u'_t} = D_{tt}\frac{\partial \overline{C}}{\partial x_t} + D_{tn_1}\frac{\partial \overline{C}}{\partial x_{n_1}} + D_{tn_2}\frac{\partial \overline{C}}{\partial x_{n_2}}, \tag{9}$$

$$-\overline{c'u'_{n_1}} = D_{n_1t}\frac{\partial \overline{C}}{\partial x_t} + D_{n_1n_1}\frac{\partial \overline{C}}{\partial x_{n_1}} + D_{n_1n_2}\frac{\partial \overline{C}}{\partial x_{n_2}}, \tag{10}$$

$$-\overline{c'u'_{n_2}} = D_{n_2t}\frac{\partial \overline{C}}{\partial x_t} + D_{n_2n_1}\frac{\partial \overline{C}}{\partial x_{n_1}} + D_{n_2n_2}\frac{\partial \overline{C}}{\partial x_{n_2}}, \tag{11}$$

where the subscripts t represents the direction (at every single spatial location) aligned with the (principal) in-plane direction of the turbulent scalar flux vector, and n_1 and n_2 are the corresponding in-plane and out-plane normal (orthogonal) directions to the turbulent scalar flux vector. These equations can be further simplified by considering the laser sheet is aligned with the source and in the middle of the room

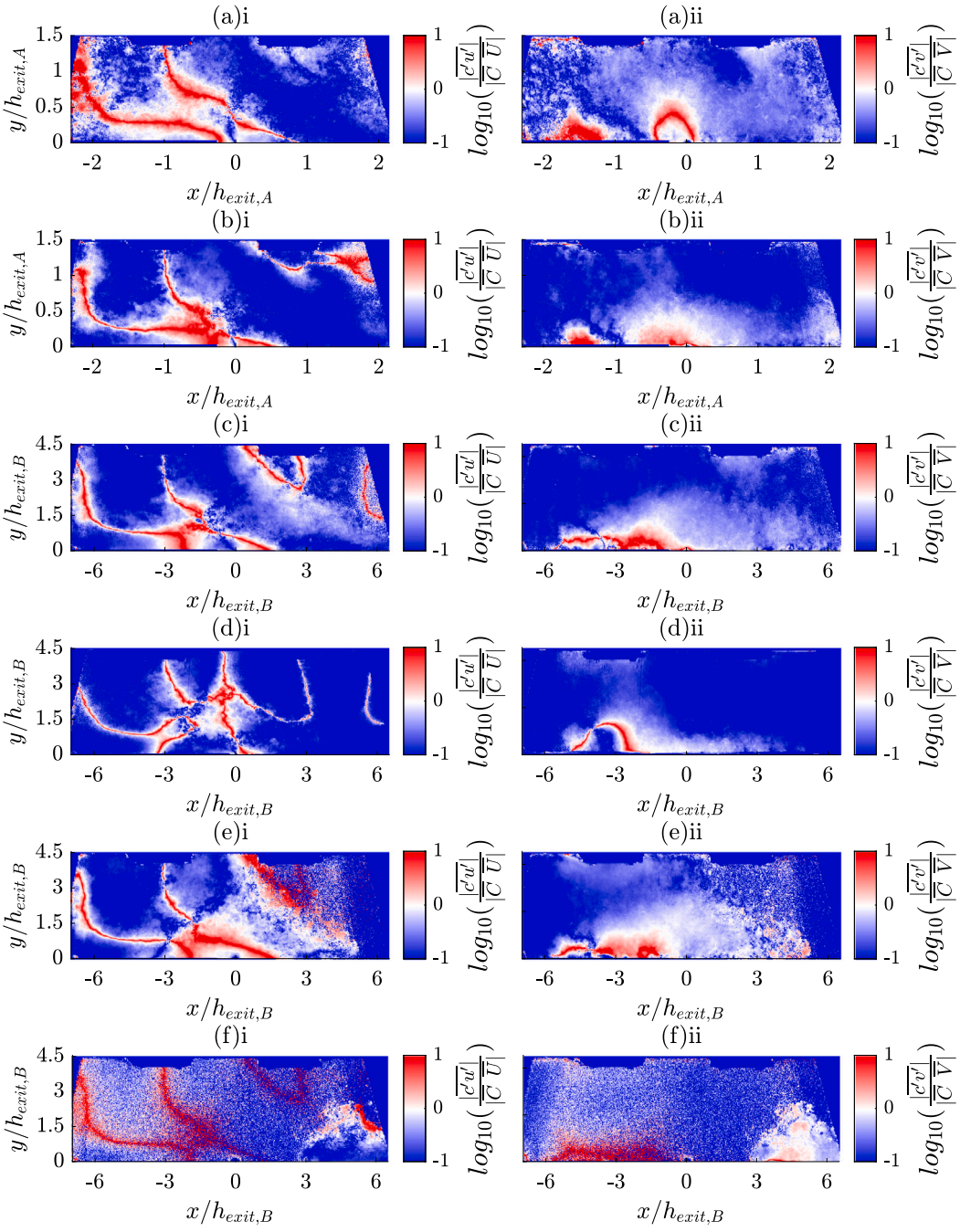

Fig. 10. Ratios of the turbulent and advective scalar fluxes for (a) A1, (b) A2, (c) B2, (d) B5, (e) B2-L and (f) B2-R test case, in the (i) horizontal and (ii) vertical directions.

(geometric symmetry) for the current study, hence there is zero mean concentration gradient and turbulent scalar fluxes in the out-plane direction (i.e., $\frac{\partial \overline{C}}{\partial x_{n_2}} = 0$ and $\overline{c'u'_{n_2}} = 0$). Furthermore, since the definition of $\overline{c'u'_t}$ is such that it is perfectly aligned with the principal in-plane direction of the turbulent scalar flux vector, the in-plane orthogonal component $\overline{c'u'_{n_1}}$ must be zero. Therefore, we are left with the following form,

$$-\overline{c'u'_t} = D_{tt}\frac{\partial \overline{C}}{\partial x_t} + D_{tn_1}\frac{\partial \overline{C}}{\partial x_{n_1}}. \tag{12}$$

In Eq. (12), D_{tn_1} is non-zero due to anisotropic turbulence in the room (i.e. misalignment of the directions of the mean concentration gradient and turbulent scalar flux vectors). To solve Eq. (12) which is an under-determined system with two unknowns in D_{tt} and D_{tn_1}, we introduce an additional constraint to regularise the problem by assuming D_{tt} and D_{tn_1} varies smoothly and gradually in space. This was implemented using a 7 × 7 moving window approach where the solutions D_{tt} and D_{tn_1} was assumed to be constant within the window. As such, each 7 × 7 window produces an over-determined set of 49 linear equations with only 2 unknowns, which was solved using Matlab's QR factorisation solver. This process is repeated for every single pixel location to solve for the entire 2D eddy diffusivity maps and follow the same procedure as that of an earlier study [11]. While it is difficult to accurately determine the uncertainties associated with introducing the additional constraint to regularise the problem, this is related to the spatial gradient of D_{tt} and D_{tn_1} which is not expected to be significant in the near-source region due to the conservative window size.

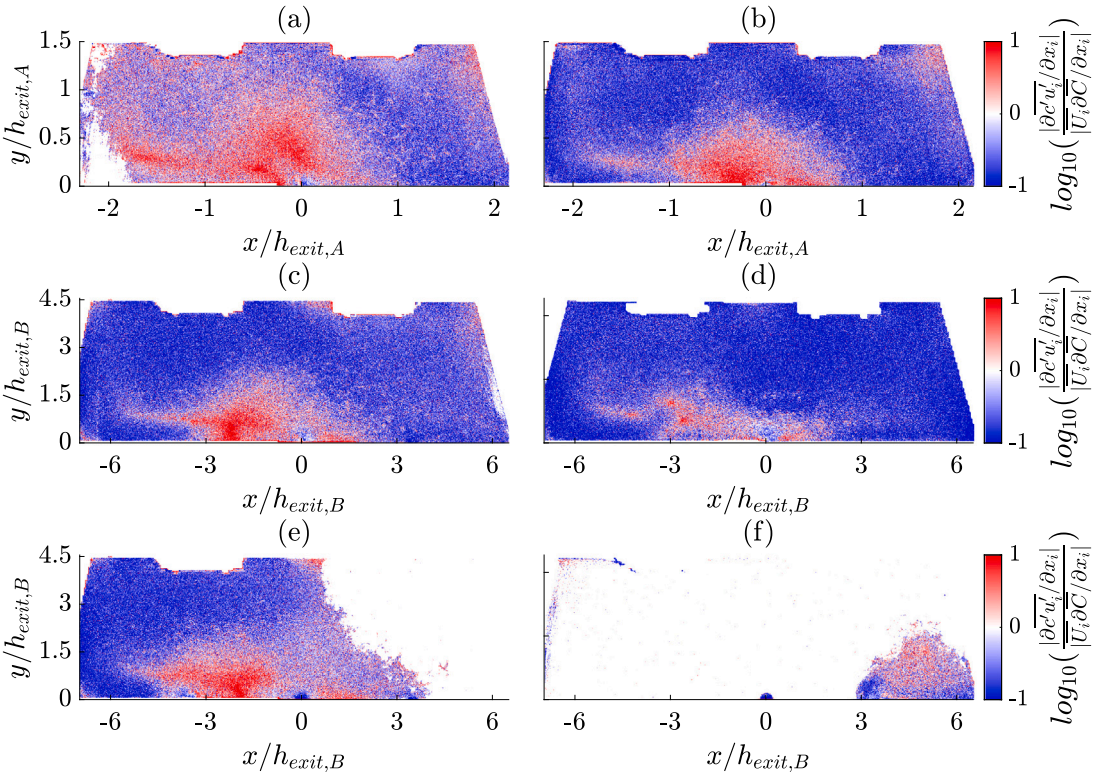

Fig. 11. Ratios of the gradients of the turbulent and advective scalar fluxes in Eq. (1) for (a) A1, (b) A2, (c) B2, (d) B5, (e) B2-L and (f) B2-R test case.

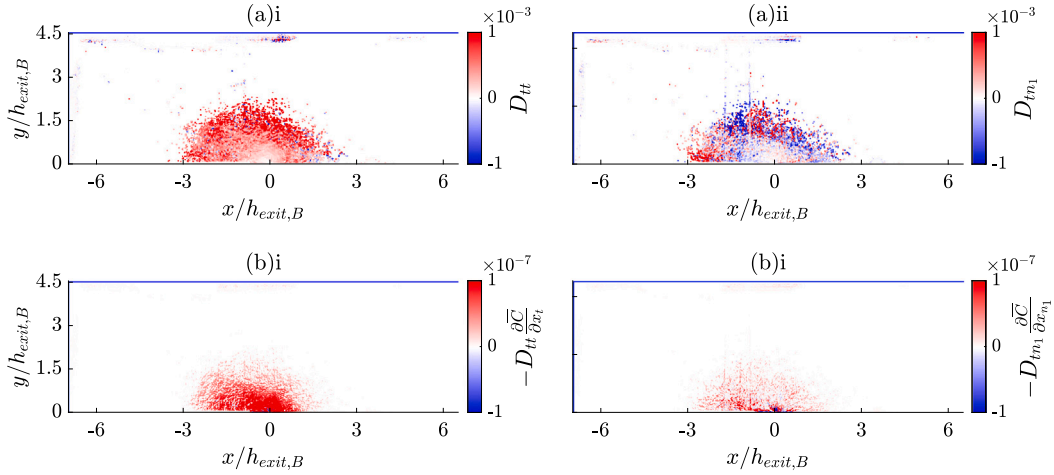

Fig. 12. Test case B2. (a) Components of the eddy diffusivity tensor and its (b) contributions to the turbulent scalar flux. (i) Tangential and (ii) normal turbulent flux-aligned directions.

The results for two test cases with the biggest qualitative differences observed in the turbulent scalar flux maps (Fig. 8) are presented in Figs. 12 and 13. Although D_{tn_1} is non-zero, its contribution to the turbulent scalar fluxes can be observed to be much lower than that of D_{tt} for both test cases as shown in Figs. 12(b) and 13(b).

5.2. An isotropic coefficient approximation

For many practical applications, it is useful to further condense the eddy diffusivity tensor maps into a single coefficient, K. As illustrated in Figs. 12 and 13, the primary contribution to $\overline{c'u_t'}$ comes from its principal component, D_{tt}. Hence, we approximate the isotropic eddy diffusion coefficient as $K \sim D_{tt}$, and we use D_{tn_1} as a way to estimate the uncertainties associated with this approximation (i.e. the errors associated with assuming isotropic turbulence and ignoring the contributions of the orthogonal component to the turbulent fluxes). To arrive at this single coefficient, spatial averaging of the maps shown in Figs. 12 and 13 is required. This is non-trivial as the shape of the turbulent fluxes is dependent on the flow field, which means methods that averages D_{tt} (and D_{tn_1}) radially or in Cartesian directions are ill-suited across the different test cases.

One way to address this is to perform conditional averaging of D_{tt} (and D_{tn_1}) for locations where the mean concentration, $\overline{C}$, is within a specified range. Here we have used bins of size $log_{10}(\overline{C}/C_s) = -4$. This results in eddy diffusivity values that are conditionally averaged only if they belong to the same mean concentration bin (see isocontour lines of the mean concentration as shown in Fig. 4). The selection of the bin size is based on a compromise between $log_{10}(\overline{C}/C_s)$ resolution and

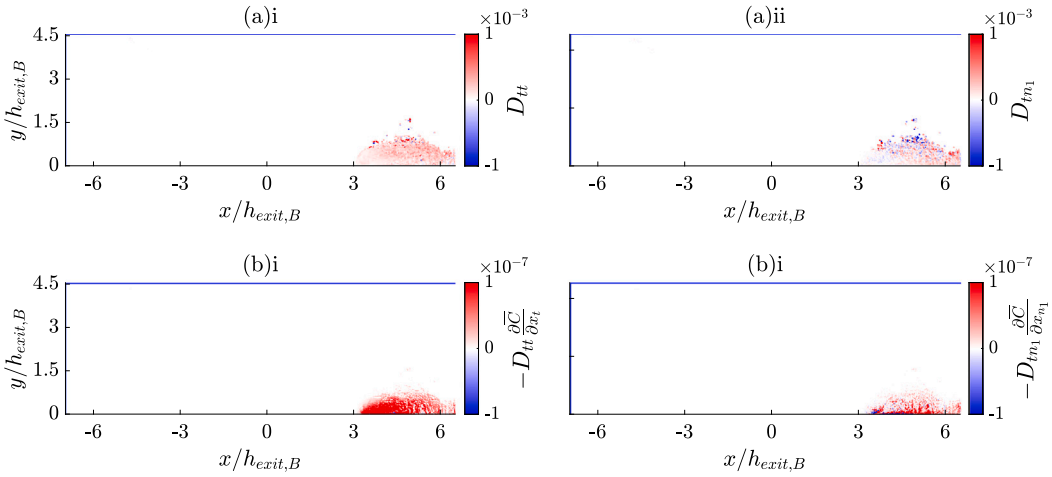

Fig. 13. Test case B2-R. (a) Components of the eddy diffusivity tensor and its (b) contributions to the turbulent scalar flux. (i) Tangential and (ii) normal turbulent flux-aligned directions.

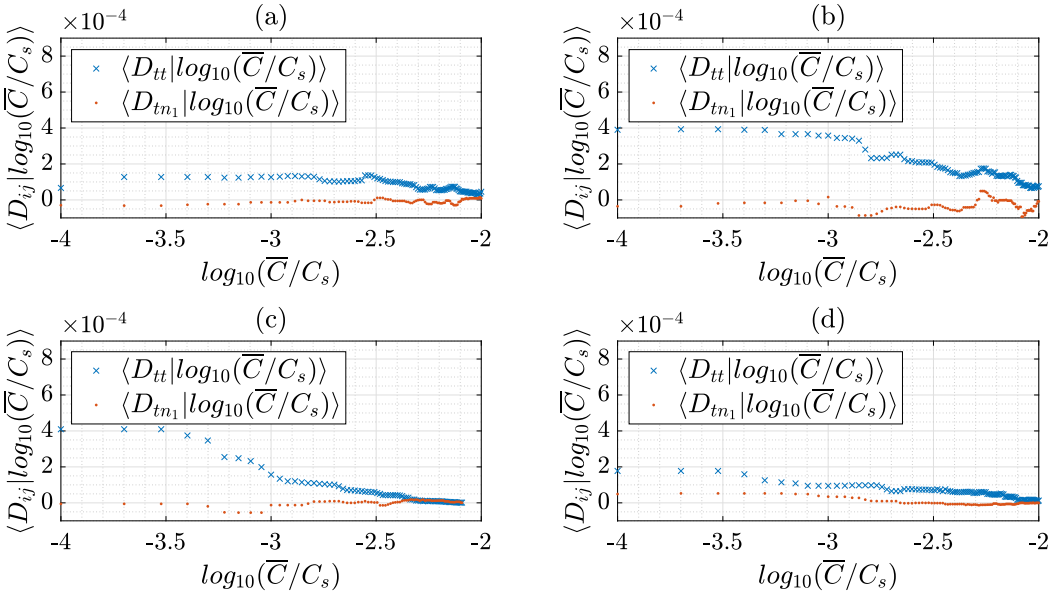

Fig. 14. The tangential (D_{tt}) and normal (D_{tn_1}) components of the eddy diffusivity tensor conditionally averaged on locations where the mean concentration is equal to a specified value of $log_{10}(\overline{C}/C_s)$ with bin sizes of $log_{10}(\overline{C}/C_s) = -4$. (a) A1, (b) A2 (c) B2, (d) B2-R test case.

robustness to noise. For instance, smaller bins have better $log_{10}(\overline{C}/C_s)$ resolution, but also offers less datapoints to average in each bin, hence are more susceptible to noise or spurious data. Larger bins oversmooth the eddy diffusivity plots and can introduce additional uncertainties if the spatial variation of the eddy diffusivity is significant. Fig. 14 shows the conditional averaged eddy diffusivity plotted against the mean concentration bins. While the mean concentration values do not necessarily represent a specific spatial location, since the shape of the isocontour lines are dependent on the flow field, higher values of mean concentration can generally be interpreted as shorter distance to the source.

Notably, there is an inverse relationship between the conditional averaged eddy diffusivity and mean concentration at higher concentration values. This could possibly be attributed to the source located at the ground-level, since turbulence length scales are expected to decrease at the near-wall region with Reynolds stresses going to zero at the wall. This hypothesis is further supported by the B2-R test case where the isocontour lines for a wide range of mean concentrations remained close to the ground, resulting in similar turbulence length scales, and hence a gentle gradient of the conditional averaged eddy diffusivity values. Much smaller values of the conditional averaged eddy diffusivity are also observed for B2-R than compared to B2, which is likely due to a lack of large-scale turbulent structures recirculating the dye back into the room given the proximity of the source to the outlet.

The final step to obtain an approximated isotropic eddy diffusion coefficient (K) is to average the values of D_{tt} presented in Fig. 14 for the mean concentration range $-3 < log_{10}(\overline{C}/C_s) < -2.5$. A fifth-order one-dimensional median filter was also applied to reduce noise. This method is in essence, a conditional averaging operation based on the mean concentration values within a specified range. The rationale to average the eddy diffusivities corresponding to relatively higher mean concentration values (i.e., $-3 < log_{10}(\overline{C}/C_s) < -2.5$) is based on the premise that they represent closer proximity to the source which in turn has a more significant role in influencing the scalar transport. In other words, eddy diffusivities at spatial locations far from the source do not matter as the mean concentration gradients there are low and do not have a significant role in the near-field transport of the scalar. Averaging was not performed all the way to the source itself (i.e., $log_{10}(\overline{C}/C_s) < -2.5$) to avoid introducing noise

Table 2
Conditional averaged isotropic eddy diffusion coefficients.

Test case	K (model) [$m^2\ s^{-1}$]	K_{FS} (full-scale) [$m^2\ s^{-1}$]	Uncertainty [%]	ACH_{FS} [h^{-1}]
A1	1.2×10^{-4}	1.8×10^{-3}	22.5	10.8
A2	2.6×10^{-4}	3.8×10^{-3}	17.5	27.4
B1	6.6×10^{-5}	1.0×10^{-3}	12.1	1.8
B2	9.4×10^{-5}	1.4×10^{-3}	12.7	1.9
B2-L	1.1×10^{-4}	1.6×10^{-3}	27.6	1.9
B2-R	8.2×10^{-5}	1.2×10^{-3}	11.0	1.9
B3	8.1×10^{-5}	1.2×10^{-3}	20.5	2.1
B4	1.0×10^{-4}	1.5×10^{-3}	14.1	2.6
B5	1.1×10^{-4}	1.7×10^{-3}	22.3	2.8

and uncertainties to the results as the number of samples for averaging rapidly decreases as the source is approached. The choice to limit the averaging to $log_{10}(\overline{C}/C_s) > -3$ is based on the mean concentration isocontour lines having already extended to almost the middle of the room in some of the test cases. In real applications where K is needed to calculate the magnitude of the turbulent scalar flux, the contribution of D_{tn_1} to the total turbulent scalar flux can be calculated using the same methodology, and used as an estimate of the uncertainty of the calculated turbulent scalar flux associated with anisotropic turbulence at the near-source region.

There are some limitations to this methodology. Since $K \sim D_{tt}$ and D_{tt} has a different direction at every spatial location, K discards information on the direction of the turbulent scalar flux vector. Nonetheless, this is acceptable as K is only needed to estimate the magnitude of the turbulent scalar flux, with the flux directions dependent on the principal direction of the mean concentration gradients. Misalignment of the principal directions of the mean concentration gradient and turbulent scalar flux is accounted for in D_{tn_1}. In addition, although the choice to conditionally average D_{tt} for the range $-3 < log_{10}(\overline{C}/C_s) < -2.5$ will introduce some uncertainties to $K \sim D_{tt}$, this is not expected to change the general trends of the results.

5.3. Discussion

The approximated isotropic eddy diffusion coefficients ($K \sim D_{tt}$) for the full range of boundary conditions investigated in this study are shown in Table 2. The uncertainties in Table 2 represent the percentage contribution of D_{tn_1} to the total turbulent scalar flux (i.e., $(D_{tn_1}\frac{\partial\overline{C}}{\partial x_{n_1}})/-\overline{c'u'_t}$). As such, for RANS applications where K_{FS} is used to estimate the magnitudes of the turbulent scalar flux using the gradient transport model (Eq. (2)), one can expect the estimated turbulent scalar flux to have an average uncertainty of around 17.8%, which is the average value across all test cases considered in this study. Generally, a linear relationship can be observed between K_{FS} and ACH_{FS} for the same room model, which can be attributed to an increase in the room turbulence at higher ACH_{FS} based on higher values of normalised velocity variances and Reynolds stress.

In comparison to the literature, our measured eddy diffusion coefficients (for room B at ACH_{FS} <2.8 h^{-1}, see Table 2) in this study (based on the advection–diffusion equation approach) are lower than the total eddy diffusion coefficients (based on the diffusion based equation) estimated by Cheng et al. [14] and Shao et al. [17]. This shows the implication of the differing definition of the 'eddy diffusion coefficient' terminology, whereby for cases where non-negligible mean flow or large-scale flow turbulence are present in the room, estimates of the total eddy diffusion coefficient obtained based on the diffusion equation approach will be greater than the eddy diffusion coefficient obtained from the advection–diffusion equation approach.

6. Conclusions and recommendations

In this study, the continuous release of a passive scalar through a ground-level point source in a 60:1 and a 20:1 full-to-model scale empty room was experimentally investigated. The ACH_{FS} and source locations were systematically varied and investigated using simultaneous PIV and PLIF techniques in a water flume facility. Mean velocity statistics show the ventilation inlets dominate turbulence production and that the normalised magnitudes of Reynolds stresses increase as the ACH_{FS} increases. The isocontour lines of the mean concentrations indicate a strong dependence on the flow field at the near-source region. Peak-to-mean concentration maps show a weak dependence on the mean concentration and concentration variance, which indicate risk may be underpredicted if based only on this information. The exponential function is a good fit to the concentration PDFs for most test cases, with the PDFs having a long right tail and the parameter C_{99}/c'_{rms} ranges between 4.5 to 5.0, consistent with the expected value of 4.61 for an exponential distribution. The exception to this occurs when the source location changes due to low/negligible concentrations measured at most of the sampled locations, although the parameter C_{99}/c'_{rms} was observed to never exceed 5.0. The universality of the exponential fit needs to be further validated with more test cases with different ventilation and source characteristics.

The spatially-resolved turbulent and advective scalar flux maps show a strong dependence of the scalar transport on the local flow field, and in particular, the importance of the local flow advection on the scalar transport. This is best exemplified by the comparison between the B2 and B2-R test cases which have the same room model and a full-scale ACH_{FS} of 1.9 h^{-1}, but drastically different scalar dispersion patterns and transport mechanisms due to the proximity of the source to the outlet for test case B2-R. The near-source flow field is particularly important as it controls the scalar transport mechanism (i.e. mean flow advection or eddy diffusion) when the concentration is high, and since the scalar fluxes decay rapidly with distance from source, the near-source flow field would have the largest influence in determining the concentration distribution. Nonetheless, the far field is expected to be important in cases where the ACH is low and the mixing efficiency is high, as this would approach the well-mixed model where concentrations are spatially uniform in the room, leading to significant scalar fluxes in the far field.

The implication of these findings for IAQ is that details (i.e. furniture, people, etc.) near to the source are important and should not be neglected as they may have a significant influence on the near-source flow field. Additionally, the assumption that the mean flow advection is negligible if ACH is low may not always be valid, and the source location and local flow field must be considered. For analytical solutions used in indoor scalar dispersion problems, it is essential to have a prior knowledge of the room flow field particularly at the near-source region, in order to facilitate the selection of the most suitable mathematical model. For instance, if the source is located in a region with strong forced advection, an advection–diffusion based model may work better than a diffusion-based model. In RANS approach, the relative contributions of the gradients of the turbulent and advective scalar fluxes affect mean concentration predictions. Larger contributions of the turbulent component is observed at the near-source region for some of the test cases, indicating the need for accurate characterisation of the eddy diffusivity at the near-source region.

The measured eddy diffusivity tensor (D_{tt} and D_{tn_1}) was redefined to align with the local turbulent scalar flux directions, and reduced to an approximated isotropic coefficient (K) by performing conditional averaging of D_{tt} in the mean concentration range $-3 < log_{10}(\overline{C}/C_s) < -2.5$. D_{tn_1} was used to estimate the uncertainty associated with the assumption of isotropic turbulence by considering its contribution to the magnitude of the turbulent scalar flux. The assumption of isotropic turbulence introduces an average uncertainty of 17.8% to the magnitudes of the turbulent scalar fluxes across all test cases. While the

ACH_{FS} has a linear and positive relationship with K_{FS}, the source location and room design can change the flow field at the near-source region significantly which influences the estimates of K_{FS}.

In this study, we have neglected the effects of human activities which can introduce additional mechanical and thermal turbulence through activities such as walking or the temperature difference between the body and the room. We have also not explored the possibility of integrating the effects of flow advection into the eddy diffusion coefficient estimates to obtain a '*total* eddy diffusivity' coefficient, which would be a better comparison with diffusion equation based methods [14,15]. We hope to explore these research directions in our future work.

CRediT authorship contribution statement

H.D. Lim: Writing – review & editing, Writing – original draft, Visualization, Validation, Software, Resources, Project administration, Methodology, Investigation, Funding acquisition, Formal analysis, Data curation, Conceptualization. **Timothy G. Foat:** Writing – review & editing, Validation, Methodology, Investigation, Formal analysis, Conceptualization. **Simon T. Parker:** Writing – review & editing, Validation, Methodology, Investigation, Formal analysis, Conceptualization. **Christina Vanderwel:** Writing – review & editing, Validation, Supervision, Software, Resources, Methodology, Investigation, Funding acquisition, Formal analysis, Conceptualization.

Declaration of competing interest

The authors declare that they have no known competing financial interests or personal relationships that could have appeared to influence the work reported in this paper.

Data availability

Data for all the quantitative maps are made available in the University of Southampton data repository at https://doi.org/10.5258/SOTON/D2932 to enable comparison and validation with future research.

Acknowledgements

The authors gratefully acknowledge the support of Christina Vanderwel's UKRI Future Leader's Fellowship, United Kingdom (MR/S015566/1) and H.D. Lim's Royal Academy of Engineering Intelligence Community Postdoctoral Research Fellowship, United Kingdom (ICRF2122-5-184).

References

[1] N.E. Klepeis, W.C. Nelson, W.R. Ott, J.P. Robinson, A.M. Tsang, P. Switzer, J.V. Behar, S.C. Hern, W.H. Engelmann, The national human activity pattern survey (NHAPS): A resource for assessing exposure to environmental pollutants, J. Exposure Sci. Environ. Epidemiol. 11 (3) (2001) 231–252.
[2] G.I. Taylor, Diffusion by continuous movements, Proc. Lond. Math. Soc. 2 (1) (1922) 196–212.
[3] G.K. Batchelor, Diffusion in a field of homogeneous turbulence. I. Eulerian analysis, Aust. J. Chem. 2 (4) (1949) 437–450.
[4] C.V.M. Vouriot, T.D. Higton, P.F. Linden, G.O. Hughes, M. van Reeuwijk, H.C. Burridge, Uniformly distributed floor sources of buoyancy can give rise to significant spatial inhomogeneities within rooms, Flow 3 (2023) E18.
[5] P. Sharma, S.S. Bahga, A. Gupta, Modeling of dispersion of aerosolized airborne pathogens exhaled in indoor spaces, Phys. Fluids 35 (4) (2023).
[6] A. Venkatram, J. Weil, Modeling turbulent transport of aerosols inside rooms using eddy diffusivity, Indoor Air 31 (6) (2021) 1886–1895.
[7] K.L. Calder, On the equation of atmospheric diffusion, Q. J. R. Meteorol. Soc. 91 (390) (1965) 514–517.
[8] S. Tavoularis, S. Corrsin, Effects of shear on the turbulent diffusivity tensor, Int. J. Heat Mass Transfer 28 (1) (1985) 265–276.
[9] C. Vanderwel, S. Tavoularis, Measurements of turbulent diffusion in uniformly sheared flow, J. Fluid Mech. 754 (2014) 488–514.
[10] T. van Hooff, B. Blocken, P. Gousseau, G.J.F. van Heijst, Counter-gradient diffusion in a slot-ventilated enclosure assessed by LES and RANS, Comput. & Fluids 96 (2014) 63–75.
[11] H.D. Lim, C. Vanderwel, Turbulent dispersion of a passive scalar in a smooth-wall turbulent boundary layer, J. Fluid Mech. 969 (2023) A26, http://dx.doi.org/10.1017/jfm.2023.562.
[12] C. Gualtieri, A. Angeloudis, F. Bombardelli, S. Jha, T. Stoesser, On the values for the turbulent Schmidt number in environmental flows, Fluids 2 (2) (2017) 17.
[13] M. Nicas, C. Keil, C. Simmons, T. Anthony, Turbulent eddy diffusion models, Math. Models Estim. Occup. Exposure Chem. (2009) 53–65.
[14] K.C. Cheng, V. Acevedo-Bolton, R.T. Jiang, N.E. Klepeis, W.R. Ott, O.B. Fringer, L.M. Hildemann, Modeling exposure close to air pollution sources in naturally ventilated residences: Association of turbulent diffusion coefficient with air change rate, Environ. Sci. Technol. 45 (9) (2011) 4016–4022.
[15] T.G. Foat, J. Drodge, J. Nally, S.T. Parker, A relationship for the diffusion coefficient in eddy diffusion based indoor dispersion modelling, Build. Environ. 169 (2020) 106591.
[16] N. Mingotti, R. Wood, C.J. Noakes, A.W. Woods, The mixing of airborne contaminants by the repeated passage of people along a corridor, J. Fluid Mech. 903 (2020) A52.
[17] Y. Shao, S. Ramachandran, S. Arnold, G. Ramachandran, Turbulent eddy diffusion models in exposure assessment-determination of the eddy diffusion coefficient, J. Occup. Environ. Hyg. 14 (3) (2017) 195–206.
[18] E. Karlsson, A. Sjöstedt, S. Håkansson, Can weak turbulence give high concentrations of carbon dioxide in baby cribs? Atmos. Environ. 28 (7) (1994) 1297–1300.
[19] P.J. Drivas, P.A. Valberg, B.L. Murphy, R. Wilson, Modeling indoor air exposure from short-term point source releases, Indoor Air 6 (4) (1996) 271–277.
[20] P.V. Nielsen, Fifty years of CFD for room air distribution, Build. Environ. 91 (2015) 78–90.
[21] Y. Li, P.V. Nielsen, CFD and ventilation research, Indoor Air 21 (6) (2011) 442–453.
[22] J.D. Posner, C.R. Buchanan, D. Dunn-Rankin, Measurement and prediction of indoor air flow in a model room, Energy Build. 35 (5) (2003) 515–526.
[23] Y. Fan, CFD modelling of the air and contaminant distribution in rooms, Energy Build. 23 (1) (1995) 33–39.
[24] C. Kandzia, D. Mueller, Flow structures and Reynolds number effects in a simplified ventilated room experiment, Int. J. Vent. 15 (1) (2016) 31–44.
[25] P.V. Nielsen, Specification of a Two-Dimensional Test Case: (IEA), in: Gul Serie, (8) Institut for Bygningsteknik, Aalborg Universitet, 1990, International Energy Agency, Energy Conservation in Buildings and Community Systems, Annex 20, Air Flow Pattern within Buildings PDF for print: 22 pp..
[26] C. Tantasavasdi, J. Srebric, Q. Chen, Natural ventilation design for houses in thailand, Energy Build. 33 (8) (2001) 815–824.
[27] G. Cao, H. Awbi, R. Yao, Y. Fan, K. Sirén, R. Kosonen, J.J. Zhang, A review of the performance of different ventilation and airflow distribution systems in buildings, Build. Environ. 73 (2014) 171–186.
[28] R.D. Keane, R.J. Adrian, Optimization of particle image velocimeters: II. Multiple pulsed systems, Meas. Sci. Technol. 2 (10) (1991) 963.
[29] H.D. Lim, D. Hertwig, T. Grylls, H. Gough, M. van Reeuwijk, S. Grimmond, C. Vanderwel, Pollutant dispersion by tall buildings: Laboratory experiments and large-eddy simulation, Exp. Fluids 63 (6) (2022) 92.
[30] W. Thielicke, E. Stamhuis, PIVlab–towards user-friendly, affordable and accurate digital particle image velocimetry in MATLAB, J. Open Res. Softw. 2 (1) (2014).
[31] T.L. Thatcher, D.J. Wilson, E.E. Wood, M.J. Craig, R.G. Sextro, Pollutant dispersion in a large indoor space: Part 1–scaled experiments using a water-filled model with occupants and furniture, Indoor Air 14 (4) (2004) 258–271.
[32] Z.J. Zhai, Z. Zhang, W. Zhang, Q. Chen, Evaluation of various turbulence models in predicting airflow and turbulence in enclosed environments by CFD: Part 1—Summary of prevalent turbulence models, HVAC&R Res. 13 (6) (2007) 853–870.
[33] M.F. King, C.J. Noakes, P.A. Sleigh, M.A. Camargo-Valero, Bioaerosol deposition in single and two-bed hospital rooms: a numerical and experimental study, Build. Environ. 59 (2013) 436–447.
[34] J. Hou, Y. Sun, Q. Chen, R. Cheng, J. Liu, X. Shen, H. Tan, H. Yin, K. Huang, Y. Gao, X. Dai, L. Zhang, B. Liu, J. Sundell, Air change rates in urban Chinese bedrooms, Indoor Air 29 (5) (2019) 828–839.
[35] C. Howard-Reed, L.A. Wallace, W.R. Ott, The effect of opening windows on air change rates in two homes, J. Air Waste Manag. Assoc. 52 (2) (2002) 147–159.
[36] H. Abid, I. Baklouti, Z. Driss, J. Bessrour, Experimental and numerical investigation of the Reynolds number effect on indoor airflow characteristics, Adv. Build. Energy Res. 14 (4) (2020) 424–449.
[37] S.A. Al-Sanea, M.F. Zedan, M.B. Al-Harbi, Effect of supply Reynolds number and room aspect ratio on flow and ceiling heat-transfer coefficient for mixing ventilation, Int. J. Therm. Sci. 54 (2012) 176–187.
[38] M. Weng, P.V. Nielsen, L. Liu, A Discussion of Low Reynolds Number Flow for the Two-Dimensional Benchmark Test Case, DCE Technical reports 116, Department of Civil Engineering, Aalborg University, Denmark, 2012.
[39] K. Zhong, X. Yang, Y. Kang, Effects of ventilation strategies and source locations on indoor particle deposition, Build. Environ. 45 (3) (2010) 655–662.

[40] T.G. Foat, S.T. Parker, I.P. Castro, Z.T. Xie, Numerical investigation into the structure of scalar plumes in a simple room, J. Wind Eng. Ind. Aerodyn. 175 (2018) 252–263.
[41] S.T. Parker, C.J. Coffey, Analytical solutions for exposures and toxic loads in well-mixed shelters in support of shelter-in-place assessments, J. Hazard. Mater. 192 (1) (2011) 419–422.
[42] W.R. Chan, W.W. Nazaroff, P.N. Price, A.J. Gadgil, Effectiveness of urban shelter-in-place—I: Idealized conditions, Atmos. Environ. 41 (23) (2007) 4962–4976.
[43] A. Chaloulakou, I. Mavroidis, Comparison of indoor and outdoor concentrations of CO at a public school. Evaluation of an indoor air quality model, Atmos. Environ. 36 (11) (2002) 1769–1781.
[44] S.C. Lee, M. Chang, Indoor air quality investigations at five classrooms, Indoor Air 9 (2) (1999) 134–138.
[45] A. Rackes, M.S. Waring, Modeling impacts of dynamic ventilation strategies on indoor air quality of offices in six US cities, Build. Environ. 60 (2013) 243–253.
[46] National Research Council (US) Committee on Acute Exposure Guideline Levels, Acute Exposure Guideline Levels for Selected Airborne Chemicals, Vol. 9, National Academies Press (US), 2010.
[47] W.F. Ten Berge, A. Zwart, L.M. Appelman, Concentration—time mortality response relationship of irritant and systemically acting vapours and gases, J. Hazard. Mater. 13 (3) (1986) 301–309.
[48] T.L. Hilderman, S.E. Hrudey, D.J. Wilson, A model for effective toxic load from fluctuating gas concentrations, J. Hazard. Mater. 64 (2) (1999) 115–134.
[49] D.W. Gaylor, The use of Haber's law in standard setting and risk assessment, Toxicology 149 (1) (2000) 17–19.